High-Aspect Ratio Au Microflakes via Gap-Assisted Synthesis

Fatemeh Kiani[1], *Giulia Tagliabue*[1]*

[1] *Laboratory of Nanoscience for Energy Technologies (LNET), STI, École Polytechnique Fédérale de Lausanne, 1015 Lausanne, Switzerland*

Abstract

Ultra-thin and extra-large single-crystalline Au micro-flakes (Au MFs) have a huge potential for applications ranging from nanophotonics to catalysis. Yet, wet chemical-synthesis approaches cannot access this size range due to the proportionality between growth time, thickness and lateral size. Concurrently, complexity and small MFs areas restrict the use of 2D template-based methods. In all case, subsequent transfer to a substrate remain challenging. Here, we demonstrate a facile, gap-assisted synthesis method that enables on-substrate growth of ultra-thin and extra-large Au MFs. In particular, using a 43 µm gap-size between two glass substrates and leveraging the directed-growth effect of halide ions, we achieve a high yield (~90%) of Au MFs on glass with lateral sizes as high as 0.25 mm and thicknesses as low as 10 nm. Interestingly, up to 25h growth-time we observe a time-independent, ultra-low average thickness of just 21 nm. A parametric synthesis study and an in-depth material characterization provide mechanistic insights into this extreme 2D growth mode. Overall, our gap-assisted approach greatly enhances the halide effect and results in a record-high aspect-ratio of $\sim 10^4$. It thus opens new opportunities for on-substrate anisotropic growth strategies that would benefit emerging optoelectronic and photoelectrochemical devices.

Introduction

Synthesis of nanomaterials with highly-controlled shape and size is at the core of many technologies as it grants control over their physical and chemical properties[1-2]. Among shape-controlled syntheses, anisotropic growth of 2D gold (Au) nanostructures, such as nanosheets[3-4], nanoplates[5-6], and micro-flakes[7-8] is of great interest. Indeed, thanks to their atomically-smooth and well-defined {111} crystallographic surfaces, these single-crystalline structures exhibit unique optical[9-11] and catalytic[12-13] properties. Importantly, on-substrate growth of extra-large (lateral size >100 µm) and ultrathin (thickness <30 nm) Au micro-flakes (Au MFs) could bridge the worlds of colloidal synthesis and nanofabrication, offering high-quality metal substrates for plasmonic sensing[14], optoelectronic[15-16] and (photo)electrochemical[13, 17-19] applications. For example, thanks to their long surface-plasmon propagation distances[20-21] and low thickness, these Au MFs could be used in high-sensitivity ATR-FTIR molecular detection systems[22-23]. Additionally, they could be leveraged to create arrays of monocrystalline plasmonic antennas with exact shape, size and crystallinity[24]. These are indeed expected to exhibit enhanced photoluminescence emission[25-26], stronger electric field enhancement[7] as well as improved generation of hot electrons[27] and their ballistic transport to a semiconducting substrate[28-29]. Overall, the combination of all these qualities would play a pivotal role both for fundamental understanding and performance improvement of emerging plasmonic devices. Yet, a synthesis method to achieve on-substrate growth of extreme aspect-ratio Au MFs is not available.

To date, many synthesis strategies have been developed to grow Au MFs by reducing chloroaurate ($AuCl_4^-$) ions with wet chemical[5], electro-chemical[30], photo-chemical[31-32], and thermal[33] reduction methods that follow a kinetically-controlled pathway. Yet, a critical disadvantage of these approaches is their lack of independent control over the thickness and lateral size of the flakes. This limits the synthesis products to rather thick (>100 nm) large-size Au MFs[33-35] or ultrathin (< 10 nm) but small-size nano-flakes[21, 36]. Recently, it has been shown that, under highly controlled growth conditions, periodical refilling of the Au precursor during the synthesis can significantly increase the aspect-ratio (i.e. lateral size over thickness) of the Au MFs[37]. However, the average thickness still proportionally increases with the growth time. Thus, breaking the proportionality between the thickness and growth time while promoting 2D lateral growth to obtain ultrathin large-size Au MFs remains a challenge (Figure 1a).

The controlled addition of halide ions (I^-, Br^-, Cl^-) during the synthesis of nanomaterials, including Au MFs, has been shown to strongly promote a 2D growth mode[38-40]. This effect has been attributed to the multiple roles played by the halide ions in both the nucleation and growth processes, including surface passivation of the Au {111} facets[40-42], complexation with the Au precursor[43-44], and oxidative etching[45-46].

However, despite the observed promising effects of halide ions on both morphological yield[45] and lateral size[34] of the MFs, the reported halide-assisted synthesis approaches were not successful in obtaining very-high (∼10^4) aspect-ratio Au MFs. Thus, while it is known how to promote the lateral growth[33-34, 47], there is still a lack of understanding and control of the conditions that can suppress the growth in the thickness direction.

Recently, space- or template-confined growth method has emerged as an effective approach for synthesizing ultrathin 2D nanostructures.[48] Indeed, the confined space restricts the growth in the out-of-plane direction and also the supply of growth precursors[48-49]. Confined-growth agents are not only limited to soft templates of bilayer liquid crystal micelles[21] and vesicles[50], but can also be layered 2D materials themselves, e.g. graphene oxide[51], and transition metal dichalcogenides[52]. To date, some ultrathin 2D metal and metal oxide nano-flakes have been synthesized by using these templates[48]. However, it is challenging to chemically remove the template after synthesis due to the strong interactions with the synthesized 2D structures[51-52]. Very recently, space-confined chemical vapor deposition inside two stacked mica substrates has been used for synthesis of ultrathin nanosheets of semiconducting compounds that can be easily transferred to any desired substrate[53-55]. However, this approach still suffers from the limited lateral size and low growth efficiency for the grown structures.

Here, we report an on-substrate gap-assisted synthesis approach that leverages the shape-directing effects of halide-ions to achieve high-yield (∼90%) of extreme aspect-ratio Au MFs with lateral sizes up to 0.25 mm and thicknesses down to 10 nm on glass substrates. Interestingly, our statistical analysis of a large number of on-substrate grown flakes shows that controlled addition of a combination of Br^- and Cl^- ions under spatial confinement (∼43 µm gap) has the most significant effect on the 2D growth mode by breaking the proportionality between growth time, thickness and lateral size (Figure 1b). In particular, we observe a promoted lateral growth rate at a time-independent average thickness of 20.6 nm for growth times up to 25 h. Our detailed characterization study provides mechanistic insights into this extreme 2D growth mode. Thanks to the simplicity of the on-substrate synthesis process and the observed unprecedented aspect-ratio of 1.1×10^4, our ultrathin and large-size Au MFs could serve as high-quality thin films for top-down fabrication of numerous nanophotonic components (i.e. optical sensors). Also, they could find broad application in nanodevices requiring transparent conductive substrates as well as in plasmonic hot-carrier optoelectronic and photoelectrochemical systems.

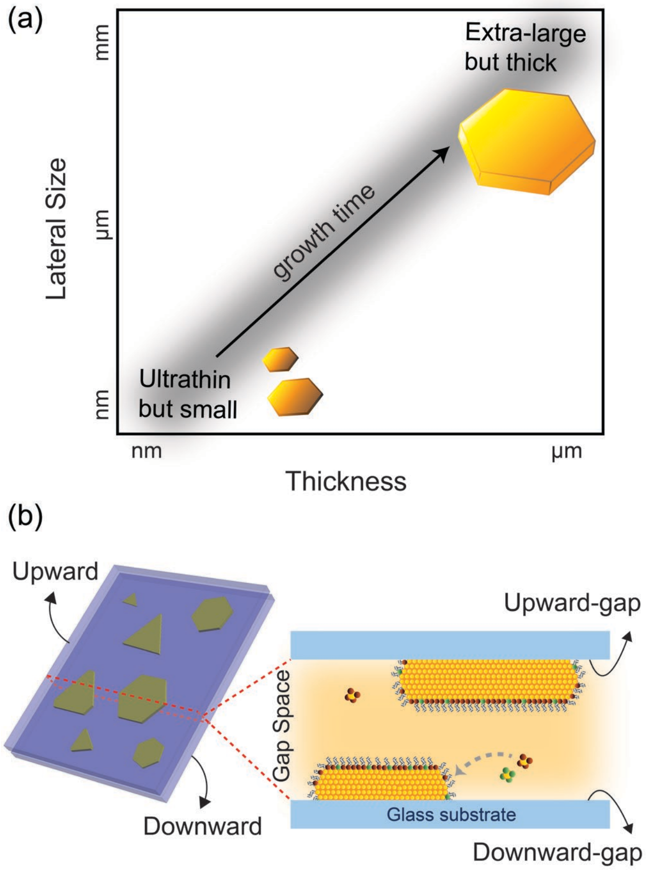

Figure 1. (a) Schematic illustration of the lateral size-thickness proportionality, pointing to the challenge in realizing ultrathin large-size Au micro-flakes. (b) Schematic diagram of the halide-assisted growth of ultrathin large-size Au micro-flakes within the confined gap space constructed by two stacked glass substrates. Red and green dots represent the halide-ions whose surface passivation and complexation effects will be shown to suppress thickness growth kinetics while enhancing lateral growth. Labelling of the studied surfaces is also indicated.

Results and Discussion

Gold MFs were grown on borosilicate glass substrates through a seedless halide-assisted polyol process. In brief, microliter amounts of aqueous KI, KBr, or KCl solutions at micromolar concentrations were added to a diluted solution of hydrogen tetrachloroaurate ($HAuCl_4 \cdot 4H_2O$) in ethylene glycol (EG) followed by subsequent heating at 90°C in a water bath (see Methods). For comparison purposes, the synthesis procedure was repeated using the same growth condition, but without adding any halide ions, a process that we will refer to as *halide-free* approach. It is to mention that even without external addition of halide ions, i.e. in our halide-free approach, in the growth solution there are still Cl^- ions from $HAuCl_4^-$. In both the halide-free and halide-assisted cases, two glass substrates were immersed vertically into the growth solution. Importantly, the substrates were first wetted by the growth solution and then placed back-to-back, leaving a 43 μm wetted gap between them. As we will see later, this space-confined region plays a critical role in the anisotropic growth of the flakes. Furthermore, the substrates were slightly tilted with respect to the vertical, creating an upward and downward facing sample which exhibit different flake adhesion characteristics (see Figure 1b and S1). Flakes formation was studied on the downward, the downward-gap and the upward-gap surfaces. After the growth period, that we varied from 8 h to 25 h, the substrates were cleaned by several rinsing with ethanol and DI water to remove the remaining reagents. Numerous Au MFs with triangular, hexagonal, or truncated triangular shapes were found on the surfaces and in the solution. Only the substrate-grown flakes, which are the focus of our study, were considered for statistical analysis. This is because of the common imperfections, e.g. small-particle-induced elevation, agglomeration, and bending, of the colloidally-grown Au MFs that appear after drop-casting them onto a substrate, resulting in serious loss of useful flake area[8]. The growth of the numerous flakes formed across the whole surface area of the substrates was quantified under an inverted optical microscope to determine their formation yield, thickness and lateral size distributions. The lateral size distribution was analyzed by measuring the side length of triangular flakes and the diagonal length of hexagonal and truncated triangular flakes from the recorded optical micrographs. The thickness distribution of the flakes was obtained via a transmission spectral method that correlates the optical transmittance measured from a CCD image to the thickness[25] (see Methods and Figure S2). All these measurements were restricted to flakes with lateral sizes larger than 10 μm. Finally, the formation yield was determined by calculating the number fraction of large-size MFs compared with other morphologies (by-products) as well as flakes smaller than 10 μm.

The results of our systematic synthesis studies aimed at identifying the optimized growth condition for high aspect-ratio Au MFs, as well as at elucidating the underlying growth mechanisms are shown in Figure 2 and Figures S5-S10. First, for the fixed growth time of 15 h, we compared a halide-free synthesis to the addition of 0.5 mM of KI, KCl, and KBr, respectively. We observe that, in all cases, flakes grown on the gap-facing surfaces had higher formation yields, larger areas and lower thicknesses than those formed outside the gap space (Figure S5). In particular, the upward-gap surface always provided the best outcome. This distinctive result can be attributed to a physical confinement effect[21, 53], which restricts the transport of $AuCl_4^-$ ions, and decreased sedimentation[37], which results in limited attachment of the reduced Au atoms and thermodynamically-stable small by-products onto the upward-gap surface. To show the effect of physical confinement of two stacked glass substrates on mass transport of the Au(III) ions, we simulated the steady-state diffusion of the Au(III) ions, i.e. $AuCl_4^-$ and/or $AuBr_4^-$ complexes, towards two 100 µm-radius Au MFs growing at the center of a gap-facing surface, i.e. downward-gap surface, and a free surface, i.e. upward surface, in a 2D axisymmetric geometry (see Supporting Information 2, and Figure S3). In particular, Figure S4c shows that the concentration of Au(III) ions along the gap-facing surface and the free surface are very different. In fact, within the gap the concentration is much lower than on the free surface, which can slow down the kinetics of the Au(III) complexes reduction inside the gap space. Thus, the extreme kinetically-controlled condition in the gap significantly promotes 2D anisotropic growth as a result of the intrinsically higher affinity of the {100} and/or {110} crystallographic planes on the side facets than the {111} planes on the basal facets for attachement of the Au ad-atoms[8]. Moreover, the observed larger depletion length for the Au(III) ions around the flake on the gap-facing surface can be equivalnet to local accomulation of the Cl^- and/or Br^- ions that realese from the reduction of Au(III) complexes in the growth solution around growth fronts of the growing Au MFs. This gap-assisted change in accumolation of halide ions can locally enhance the kinetically controlled condition around the growth fronts of the Au MFs based on the chemical equilibrium principle for the reduction of $AuCl_4^-$ and/or $AuBr_4^-$ complexes and thus increase their lateral growth rate[56]. More importantly, the diffusive flux arrows in Figures S4a,b show that the diffusion of Au(III) ions on the free surface is isotropic, both parallel and perpendicular on the substrate, while it is highly directional and parallel to the substrate in the gap space. This directional diffusion of the Au(III) ions can specifically enhance the growth kinetics in the lateral direction for the flakes grown inside the gap space while limiting the growth in the thickness direction.

In the absence of halide ions, truncated triangular and nonequilateral hexagonal Au MFs with an average lateral size and thickness of 60 µm and 45 nm, respectively, formed on the upward-gap surface with a ~60% yield (see Figure 2a). As observed in previous studies on Au nanoprisms[38, 45, 57], the addition of KI strongly suppressed the growth of Au MFs and led to the formation of a large number of small-sized (< 10 µm) flakes, considered as by-products in our study. In contrast, separate addition of KCl and KBr significantly promoted the formation of Au MFs by increasing their formation yield (~78%) and lateral sizes (65 µm and 73 µm, respectively) while simultaneously decreasing their average thickness to ~23 nm[41] (Figure 2a). Hence, the presence of halide ions plays a major role in tuning the yield and dimensions of the Au MFs.

Although several effects of halide-ions, such as surface passivation and complexation, are well-known, they have not been studied in the context of on-substrate Au MFs growth before. To gain a deeper knowledge of the role of Cl^- and Br^- ions in the MFs formation, we varied KBr and KCl concentrations from 0.1 mM to 50 mM (Figure S6 and S7). We observe that even the addition of an extremely small amount (0.1 mM) of Br^- ions to the growth solution drastically decreases the average thickness of the flakes. Importantly, at a Br^- concentration of 0.5 mM, such thickness reduction happens together with a huge increase in the lateral size of the flakes. By further increasing the Br^- concentration to 5 mM and 50 mM, both the yield and lateral size of the flakes decreased significantly. The concentration-independent thickness suggests that the saturated surface passivation role of the Br^- ions on the top {111} basal plane of the flakes controls the thickness growth[58]. Also the decreased lateral size at high Br^- concentrations indicates that the lateral growth is predominantly affected by complexation and oxidative etching effects, which get stronger with Br^- concentration[43, 46]. The study results on the effect of KCl concentration in Figure S7 generally show very similar trends for the formation yield, lateral size and thickness of the flakes, with the only exception of the increased formation of nanorods at high concentrations of Cl^- ions (Figure S7e) instead of small-particle by-products observed under the condition of excessive Br^- ions (Figure S6e). Accordingly, the optimum concentration of Cl^- ions was found to be also 0.5 mM, and any increased addition of Cl^- ions at 5 mM or 50 mM was detrimental to the 2D lateral growth and thus the yield of the Au MFs. Similar to the complexation effect of Br^- ions, addition of Cl^- ions affects the chemical equilibrium of the reduction process of $AuCl_4^-$ ions and slows it down, enhancing the kinetically controlled growth condition[56]. We also note that recent studies reported a strong effect of different halide surface-complexes on the Fermi level of the metal[59]. This could indeed contribute to the observed morphological and growth-rate differences when combined with an auto-catalytic process for Au seeds growth and anisotropic adsorption of halide ions on different crystal facets. A complete discussion on the effect of the halide ions can be found in Supplementary Information S3.

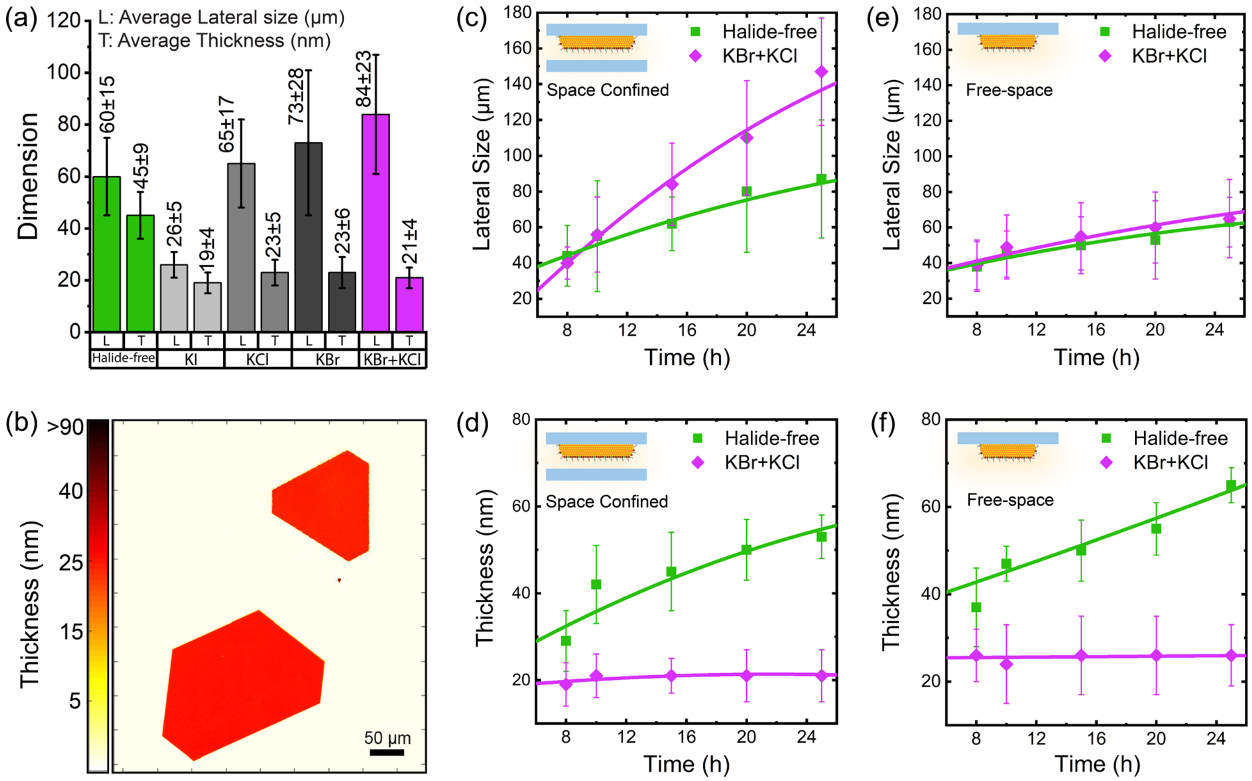

Figure 2. Effect of halide ions and space confinement on the lateral size and thickness of Au micro-flakes. (a) Bar diagram showing the measured average lateral size and average thickness for the flakes grown by the halide-free, KI, KBr, KCl, and KBr+KCl-added recipes on the upward-gap surface. Halide-added samples were obtained by adding 0.5 mM aqueous solutions of halide ion salts to the growth solution, and after a growth time of 15 h. (b) CCD transmission image of two Au micro-flakes grown by adding a controlled combination of KBr and KCl. (c-f) Average lateral size and thickness against growth time for the halide-free and KBr+KCl-added samples grown on the (c,d) upward-gap and (e,f) downward (free-space) surfaces, as indicated in the schematic inset.

Based on the results of the concentration-dependent studies, a controlled combination of KBr and KCl (50 µl KBr and 50 µl KCl at 0.5 mM each) was identified that results in an extremely high yield (~90%) of Au MFs with even larger lateral sizes and much decreased thicknesses than those obtained by separate controlled addition of KBr or KCl (Figure 2a). While the complete statistical analysis of this synthesis can be found in Figure S10, Figure 2b shows a CCD transmission image of two typical Au MFs grown in these optimized conditions. The flakes are 250 µm and 163 µm in size and their uniform optical transmittances indicate uniform thicknesses of 23 nm and 22 nm, respectively, corresponding to aspect-ratios of

1.1×10^4 and 0.7×10^4. As evident from Figure S10a, the synthesis product consists of Au MFs with lateral sizes up to 0.25 mm and thicknesses down to 10 nm. It is to note that even thinner flakes (7.5 nm) were observed in another experiment performed at the same growth conditions (data not shown here). To better understand the progression of the 2D growth mode, we performed a series of time-dependent studies (growth periods of 8, 10, 15, 20, and 25 h). Figure 2c,d show the correlation between the average lateral size, thickness and growth time for the flakes obtained on the upward-gap surface with and without adding the appropriate combination of KBr and KCl. As evident, without external addition of halide ions (green curves), both the lateral size and thickness of the flakes increased proportionally with the growth time, which is a common observation for 2D Au nanostructures[34, 37, 60]. Instead, upon adding the optimal combination of Br^- and Cl^- ions (purple curves) we observe a complete suppression of the thickness growth kinetics, i.e. time-independent thickness, and an accelerated lateral growth for all studied surfaces (see also Figure S8). Such result can also be visualized by noting the constant color contrast of the CCD images of the flakes grown at different growth times (Figure S9). This remarkable observation of broken proportionality between thickness and growth time with a promoted lateral growth rate has not been reported so far. Importantly, by comparing the upward-gap and downward surfaces (Figure 2c-f), we observe that growth under spatial confinement quadruplicates ($\sim$4.4 times) the lateral growth rate while reducing the thickness by >20%, resulting in the very low average value of 20.6 nm. Thus, although halide-ions play the dominant role for realizing a time-independent thickness, spatial confinement synergistically acts with their shape-directing effect providing better kinetically-controlled growth conditions and enhancing the 2D growth mode. As a result, synthesis in the gap leads to ultra-thin and extra-large flakes with extreme aspect ratios. Indeed, on the upward-gap surface the average aspect-ratio of the flakes grows from 1.9×10^3 at 8 h to 0.7×10^4 at 25 h. This key advantage of our halide-assisted approach is quite promising for independent control of thickness and lateral size and can be employed for achieving ultrahigh-aspect-ratio Au MFs at prolonged growth times[34] or by continuing the growth in a new solution in case of depletion of the Au precursor that may slow down or even stop the lateral growth[8, 37]. We performed one-way anova analysis to compare the statistical significance of the thickness and lateral size datasets between the downward and upward gap surfaces (see Supporting Information S4). Our analysis results confirm that despite the broad size distribution that often results in large error bars, our data are statistically significant and the gap uniquely increase the lateral growth rate while decreasing the average thickness and improving the uniformity of the thickness distribution of the flakes.

To further understand the mechanism of this promoted anisotropic growth, a complete characterization of the flakes grown under optimized conditions was performed using transmission electron microscopy

(TEM), energy dispersive x-ray spectroscopy (EDS), x-ray diffraction (XRD), and x-ray photoemission spectroscopy (XPS). Here we summarize the main results while a complete discussion can be found in Supplementary Information S5. TEM analysis was performed both on the planar and cross-sectional areas of the Au MFs (Figure 3). The ultra-thinness and thus electron-transparency of the flakes facilitated the analysis process and improved the image quality. Because of both the difficulty of wet-transferring substrate-grown MFs on a TEM grid and the possibility of introducing organic contaminants during such process, for the TEM analysis on the edge of the flake we drop-casted flakes grown in the solution during the same synthesis process that led to the substrate-grown ones. Instead, cross-sectional analysis was performed on a lamella obtained from a substrate-grown flake (see Methods and Figure S17a,b).

High-resolution TEM (HRTEM) images (Figure 3c) of the top surface of the flake show highly ordered and periodic lattice fringes with an interplanar spacing of ~1.4 Å that continues up to the most exterior edge atoms. This fringe spacing can be assigned to {220} lattice planes of face-centered cubic (fcc) Au, attesting to the single-crystallinity of the flake[61]. The image also reveals that the side facet is not atomically-smooth with fully formed atomic rows but rather contains a lot of ad-atoms. This points to the controlling role of side facets in the 2D lateral growth of the flake[62]. Furthermore, selected area electron diffraction (SAED) pattern along the [111] zone axis reveals the presence of 6-fold symmetric spots. These include two sets of six strong intensity {220} and {422} reflections, expected for a [111]-oriented fcc-Au crystal, and six faint 1/3 {422} *forbidden* reflections, which are typically observed for 2D metal nanostructures[10, 60, 63] and attributed to parallel twins or stacking faults in the ⟨111⟩ direction[61-62, 64]. The absence of other reflections in the SAED pattern and the strong XRD diffraction peak at 38.3° (Figure S18) confirm that the Au MF is a single crystal with {111} facets as basal planes[21, 63, 65]. Cross-sectional HRTEM images and SAED analysis of the flake (Figure 3g-h) also support these observations. Indeed, the flake exhibits a fully crystalline structure with three twin boundaries that extend parallel to its basal planes, mirroring the {111} lattice planes of fcc-Au with a spacing of 2.4 Å [21, 66].

On the flake edge (Figure 3b), bright-field HRTEM, which has an advantageous mass-thickness contrast, reveals a continuous and ultra-smooth adsorbed layer with a thickness of ∼1.9 nm (lighter contrast area). HRTEM image of the same region (Figure 3c), however, lacks any trace of such adsorbed layer, indicating an amorphous nature. Furthermore, cross-sectional STEM image of the top basal plane (Figure 3e) shows an ultra-smooth ∼1.5 nm-thick adlayer along the entire flake. Interestingly, high magnification STEM image of this region (Figure S17c, purple dashed rectangle in Figure 3e) reveals an ultra-smooth surface, free of ad-atoms, suggesting a layer-by-layer growth mode on this facet[8]. Based on the EDS analysis

(Figures 3j, S15, and S16), which shows uniform coverage of the top basal plane with C, O, Cl, and Br elements, we infer the presence of a double organic-halide adlayer on top flake surface[46, 67]. In particular, from the EDS spectrum peaks at 1.48, 2.62, and 2.80 keV, (Figure 3k), we estimate a concentration of Br and Cl of 3.0% and 0.6%, respectively. The higher concentration of Br with respect to Cl (~5 times) is consistent with the higher affinity of Br ions for adsorption onto the Au {111} facets during the growth process[58, 68-69]. Further, detailed XPS analysis (see Supplementary Information S5 and Figure S19e-f,h-i) of the flakes reveals the presence of EG and oxidized EG molecules, adsorbed during the synthesis process[3, 9]. These thus constitute the amorphous organic layer identified by TEM analysis[70-72].

Atomic-resolved HRTEM and STEM images of the bottom basal plane (red dashed rectangle in Figure 3e, Figures 3f and S17d) also show an atomically smooth surface. Most remarkably, the absence of a lighter contrast in the bright-field HRTEM image (Figure 3f) suggests that, in contrast to the top basal plane and edge sites, no interlayer is present at the Au flake/glass substrate interface. The absence of Br and Cl peaks (11.91 and 2.62 keV) in the EDS spectrum of this region (Figure S17f) further supports the observation that the bottom basal plane of the flake is free of any halide and organic ligands. This unexpected result suggests the hypothesis that in our synthesis both the nucleation and growth of the flakes happen directly on the substrate rather than in solution. Yet, additional studies will be required to fully elucidate the early stages of this growth process.

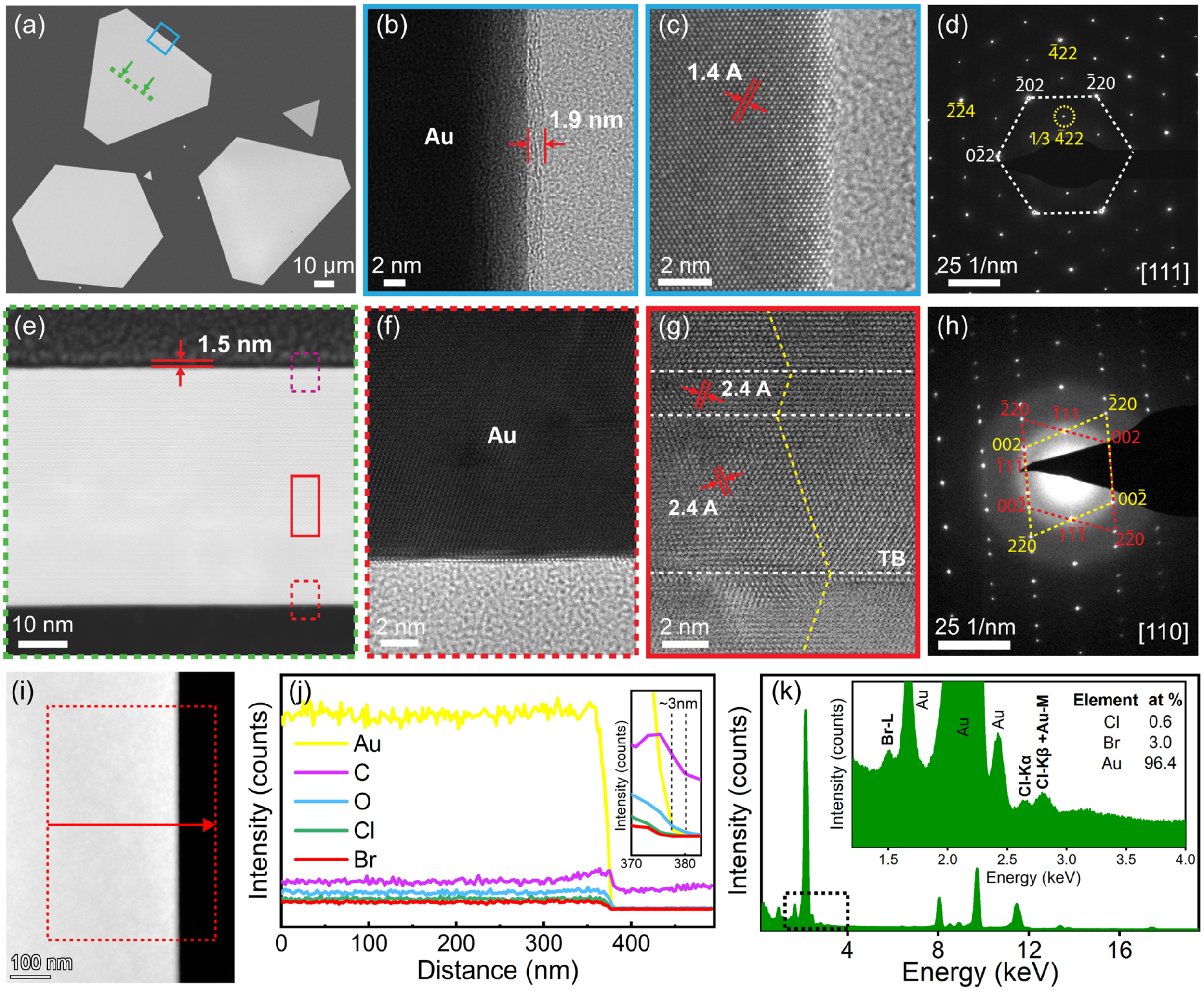

Figure 3. Planar and cross-sectional TEM/EDS results of individual Au micro-flakes grown by adding the optimized concentration of KBr and KCl. (a) Top-view SEM image of the Au micro-flakes showing the studied regions on an individual flake. (b) Planar-view BRTEM image of the edge of a solution-grown Au micro-flake marked with a blue rectangle in (a). The 1.9 nm-thick continuous organic layer on the side facet of the flake is indicated on the image. (c) Atomic-resolved HRTEM image and (d) SAED pattern of the same region taken along the [111] zone axis. The 1.4 Å spacing between the {220} planes of fcc-Au and diffraction spots are labeled correspondingly. (e) Cross-sectional STEM image of a substrate-grown Au micro-flake after FIB cross-sectioning at the region marked with a green dashed line in (a). The 1.5 nm-thick continuous organic layer on the top basal facet of the flake is labeled on the image. Atomic-resolved STEM image of the region of the purple dashed rectangle is shown in Figure S17c. (f) Atomic-resolved HRTEM image of the flake-glass substrate interface region marked with a red dashed rectangle in (e). (g) Higher magnification HRTEM image and (h) SAED pattern of the twinned region of the flake within the red

rectangle in (e) taken along the [110] zone axis. The 2.4 Å spacing between the {111} planes of fcc-Au, the {111} twin boundaries, and the mirrored diffraction spots are labeled correspondingly. (i) STEM image, (j) EDS line scans of Au, C, O, Cl, and Br elements, and (k) EDS spectrum obtained from the edge of the Au micro-flake studied in (b) and (c). The insets in (j) and (k) show a magnified view of line scans of the elements right at the edge of the flake and the EDS spectrum at an energy range of 1.2-4 keV, respectively. Atomic percent of Cl, Br and Au elements are reported after subtracting the contributions of Cu, C and O elements that mainly originate from the carbon-coated Cu grid.

On the basis of the above analysis, a possible mechanism can be proposed for the observed thickness-independent growth of high-aspect-ratio Au MFs through our halide- and gap-assisted approach (Figure 4a). Without adding any halide ions, faceted Au seeds are initially formed on the glass substrate as a result of the low reducing power of aldehyde groups (-CHO) of the heated EG, i.e. C_2H_4O, for the $AuCl_4^-$ ions, and the preferential adsorption of the in-situ formed oxidized EG molecules on the top {111} facets (see equations I and II in Figure 4a)[3, 9, 73]. Although an epitaxial relation is not possible between the Au seeds and the amorphous glass substrate, a preferred nucleation of Au seeds with [111] orientation perpendicular to the substrate can be favored due to surface energy-related minimization of the energy barrier for heterogeneous nucleation[74]. Moreover, only those seeds that are multiple twinned with their {111} twinning planes parallel to the underlying substrate can grow into in-plane Au MFs[66]. The others will either stop to grow or will grow into out-of-plane flakes that are easily washed off during rinsing with ethanol and DI water after the synthesis process[8, 33]. We note that, while on the outer surfaces we occasionally observed some out-of-plane flakes, we have never observed them inside the gap. Adsorption of the EG molecules on the [111]-oriented seeds results in a kinetically controlled condition and leads to continuous growth of the Au MFs in the lateral direction as a result of the intrinsically higher affinity of Au ad-atoms to attach to the more energetically favorable {100} and/or {110} crystallographic planes on the side facets with 4 neighboring atoms than the {111} planes on the basal facets with 3 neighboring atoms[2, 75-76]. Since the adsorbed organic layer is permeable to the diffusion of the free $AuCl_4^-$ ions to the top Au {111} facet, especially at the edges of the flake where the mean free passage time for ions are shortest[77], it incompletely passivates this facet and thus a continuous growth is also observed in the thickness direction of the Au MFs in a halide-free condition[67]. On the other hand, by adding a controlled combination of KBr and KCl at an optimized concentration, Br^- and Cl^- ions selectively adsorb onto the top {111} facet of the Au seeds and form a halide adlayer beneath the adsorbed organic layer on the top facet with a significantly higher adsorption degree for the Br^- ions[46, 58, 60, 69, 78]. This organic-halide double layer strongly suppresses the growth kinetics of the top Au {111} basal facet by acting as a diffusional barrier for surface diffusion of the $AuCl_4^-$ ions or Au adatoms on this facet, and promotes growth along the side facets less covered with the halide ions layer[40, 42, 78]. In addition to the surface passivation effect, Br^- and Cl^- ions can also interact with the Au precursor complex and increase its ionic stability[43, 79]. Bromide ions due to their higher affinity for ionic Au, can replace the Cl^- ions from the $AuCl_4^-$ complex and form a more stable $AuBr_4^-$ complex instead with a lower reduction rate, i.e. slower kinetics, as evident from its lower reduction potential[39, 46, 79] (Equation III). Similarly, as the reduction process of $AuCl_4^-$ is accompanied by the release of Cl^- ions (Equation IV), according to the chemical equilibrium principle, the added Cl^- ions can contribute to slow down the reduction process of the free $AuCl_4^-$ ions[56]. These complexation effects of Br^- and Cl^- ions synergistically provide a promoted kinetically controlled growth condition which boosts the anisotropic growth of Au MFs in the lateral direction[43, 56, 60]. This promoted lateral growth may also be attributed to the decreased supersaturation of Au atoms. The resulting kinetic inhibition of homogenous nucleation of small Au NCs in the growth solution retards the depletion of the Au precursor for the flake formation on the substrate [44], which prevents the lateral growth rate of the Au MFs to decrease over time during the synthesis process[37]. On the other hand, space confinement effect in the gap space between the substrates limits the diffusional transport of Au(III) ions from the bulk solution into the gap space and results in a highly depleted region of Au(III) ions and local accumulation of Cl^- and/or Br^- ions at the growth front of the growing Au MFs that further increase the kinetically controlled growth condition and thus the lateral growth rate of the flakes. More importantly, the highly directional diffusion of the Au(III) ions in the gap space can strongly enhance the kinetics of the lateral growth of the Au MFs on the gap-facing surface while the thickness growth kinetics is still suppressed. The overall consequence of the bimodal effects of halide ions, i.e. surface passivation and complexation, and the space confinement effect is the observed exceptional growth of extra-large and ultrathin Au MFs with a time-independent thickness.

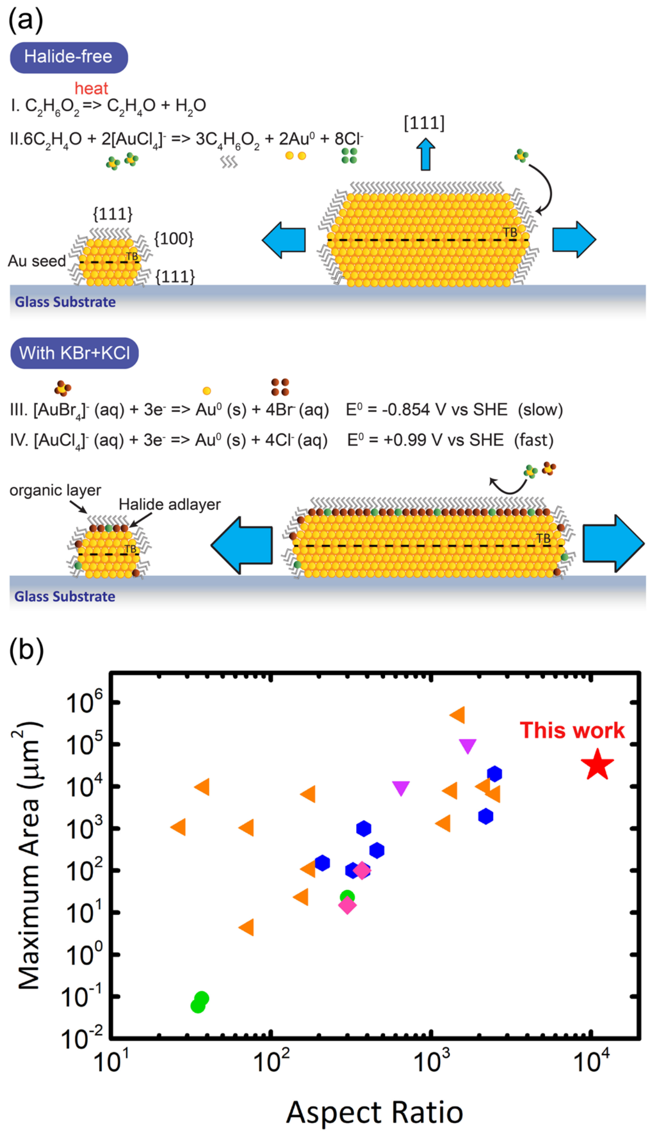

Figure 4. (a) Schematic illustration of the growth mechanisms through the halide-free (top) and halide-assisted (bottom) approaches. In the halide-free case, incomplete passivation of the top {111} basal facet of the Au seeds leads to a time-dependent thickness during the 2D lateral growth. The addition of an optimized concentration of KBr and KCl entails complete surface passivation of the top {111} facet of the Au seeds and the formation of a more stable Au-Br complex. These synergistically promote a kinetically controlled growth condition that results in time-independent growth of extreme aspect-ratio Au micro-flakes with ultrathin thicknesses. The blue arrows indicate the growth rate of the side and basal facets. (b) Comparison of maximum area and aspect-ratio of the Au micro-flakes synthesized by our halide-assisted approach (red star) with the ones previously obtained by using halide ions (green), polyol process (blue), air-thermolysis (purple), soft templates (pink) and biomolecules (orange). References are reported in Table S1.

Conclusions

In summary, we reported a facile on-substrate, gap-assisted polyol synthesis for Au MFs that uniquely enhances the shape-directing effect of halide-ion and breaks the proportionality between growth-time, lateral size and thickness. Indeed, we showed that an optimized combination of Br^- and Cl^- ions results in a high-yield (∼90%) of on-substrate Au MFs with an ultra-low, time-independent average thickness and a lateral size that, instead, increases with growth-time. Furthermore, we showed that synthesis in a 2D confined space improves control on the reaction kinetics, with a strong boosting effect on the lateral growth rate (∼4 times increase) and a limiting effect (>20% decrease) on the average thickness. Our time-dependent synthesis study, finite-element simulation, and in-depth material characterization suggest that this promoted 2D growth mode originates from the restricted and directional supply of the growth precursors in the gap space, i.e. depletion and parallel diffusion of Au(III) ions to the gap-facing surfaces, as well as halide-induced formation of stable Au(III) complexes, i.e. an enhanced kinetically-controlled condition, and selective adsorption of a continuous halide/organic bilayer on the top {111} basal facet of the Au flakes. Overall, our approach results in Au MFs with an unprecedented average aspect-ratio of $\sim 10^4$ at the growth time of 25 h, which is about 3.7 times larger than those previously obtained for giant Au MFs (see Figure 4b). We suggest that such a high aspect-ratio, occurring at a large planar area of 3.2×10^4 µm^2 and an ultrathin time-independent average thickness of ∼21 nm, can be further increased by prolonging the growth time or by employing regrowth[8] or refilling[37] methods. Thanks to their single-crystallinity, atomically-smooth and large-area surfaces, ultra-thinness, and optical transparency, our Au MFs are highly promising for top-down nanofabrication of high-quality plasmonic nano-antenna arrays[7, 9, 16] and for nanophotonic devices requiring transparent conductive substrates[80]. Also, we envision that, if confirmed by further studies, the ligand-free bottom surface of our Au MFs could serve as a unique platform for high-sensitivity single-molecule sensing[14, 81] (i.e. surface enhance Raman spectroscopy) and catalysis[12-13, 19]. Concurrently, the possibility to use other smooth substrates, such as quartz and silicon, broadens the applicability of this method. Overall, our gap-assisted synthesis approach points towards rich opportunities in exploring the synergistic use of space confinement and halide ions for on-substrate shape-controlled synthesis of nanomaterials.

Experimental Section

Synthesis recipe. Au MFs were directly grown on ultrasmooth borosilicate glass substrates (24 mm × 24 mm #1.5, VWR) by controllably adding halide ions to a halide-free synthesis recipe reported in [37]. Our seedless halide-assisted synthesis approach is based on a kinetically-controlled polyol process in which heated EG (99.8%) acts as both solvent and reducing agent and halide ions act as shape-directing agents. 40 µl of a 0.5 M aqueous solution of $HAuCl_4$ and 50 µl of KI (99.8%), KBr (≥99%), or KCl (≥99%) aqueous solutions (0.1, 0.5, 5, and 50 mM) were first added to 20 ml ethylene glycol in a polypropylene centrifuge tube (Greiner Bio-One, 50 ml) at room temperature to study the effect of each halide ion species in the growth solution. All of the chemical reagents were analytical grade, and used as received from Sigma-Aldrich. Two glass substrates were cleaned sequentially within an ultrasonic bath of acetone and ethanol for 10 min each, and immersed into the growth solution one-by-one and back-to-back in a tilted upward orientation so that the growth solution entered into the confined gap space between the two substrates. The gap size between the two wetted glass slides was estimated ~43 µm by measuring the focal plane distance between the flakes on the upward-gap and the downward-gap surfaces. Then, the solution was mildly stirred for 1 min and the capped tube was heated at 90 ˚C in a light-tight water bath on a hot-plate for 8-25 h without stirring. After the growth period, the stacked substrates were taken out of the solution at the growth temperature and washed thoroughly by rinsing with ethanol and DI water to remove the loosely attached MFs and the remaining reagents. Nitrogen blowing was used to dry the samples before further characterization. In addition to their formation in the solution, MFs were grown both on the exterior surfaces and the interior surfaces of the substrates inside the gap space. Among all the conditions, the highest aspect-ratio and the highest formation yield were observed for the flakes grown on the upward-gap surface of the top substrate by adding a controlled combination of 50 µl of KBr and 50 µl of KCl aqueous solutions (0.5 mM) to the growth solution.

Material Characterization. Optical micrographs were recorded on a customized NanoMicroSpec-Transmission™ system from NT&C. In particular images were acquired in the inverted optical microscope setup (Nikon Ti2A) combined with an imaging spectrometer (Princeton Instruments) equipped with a Peltier-cooled 2D CCD detector. Image analysis was performed on the micrographs using the open-source ImageJ software (Ver. 1.8). Atomic force microscopy (AFM) images and height profiles were obtained by using a Bruker, Fast-Scan AFM in the ScanAsyst™ mode and at a scan rate of 1 Hz. Scanning electron microscopy (SEM) was performed on a field-emission ZEISS GeminiSEM 300 with an accelerating voltage of 3 kV and working distance of 6 mm. Because of the insulating glass substrate, a thin carbon layer was sputter-coated onto he samples before SEM study. Transmission electron microscopy (TEM) analyses were carried out on a double aberration-corrected FEI Titan Themis operated at 300 kV, in both the [111] and [110] crystal directions of the Au MFs. TEM samples for planar-view studies, i.e. along the Au [111] zone axis, were prepared by drop casting a few drops of an ethanol-based (≥99.8%) suspension of solution-grown Au MFs onto a thin amorphous carbon layer supported by a Cu grid. The suspension was obtained by washing the loosely attached Au MFs on the glass substrate with ethanol after the synthesis process. Cross-sectional studies, i.e. along the Au [110] zone axis, were performed on a TEM lamella prepared from a cleaned substrate-grown Au MF with a focused ion beam (FIB)/SEM dual-beam instrument (Zeiss NVision 40). Before FIB milling, the sample was coated with a thin (~17 nm) nanocrystalline platinum layer to make it conductive. However, as the sample was still charging, a thin carbon layer (~20 nm) was sputter coated on the surface. The region of interest was then protected by FIB-assisted carbon deposition (~1 µm). Then, a chunk of the obtained a-SiO_2/Au(111)/nc-Pt/C stacked structure was extracted by FIB milling (30 kV Ga^+ beam) and attached to a TEM grid. Beam-induced damages of the surfaces were limited by thinning of the structure with a 2 kV accelerating voltage of the Ga^+ beam. X-ray diffraction (XRD) was conducted directly on substrate-grown Au MFs on a Panalytical Empyrean diffractometer equipped with a Cu k_α radiation source ($\lambda = 1.54060$ Å; 40 kV, 30 mA) and a PIXcel-1D detector. X-ray photoelectron spectroscopy (XPS) analyses were performed using a PHI VersaProbe II scanning XPS microprobe (Physical Instruments AG, Germany) equipped with an Al K_α radiation source ($h\nu = 1486.6$ eV) with a beam size of 100 µm and a hemispherical analyser. The measurements were performed on a large-size Au MF in before and after the washing treatment with ethanol and DI water, and the scan steps were 0.8 eV and 0.2 eV for the survey and high-resolution XPS spectra, respectively. All the binding energy and atomic percent values were determined by referring to the theoretical C1s line at 284.5 eV and using PHI Multipak software (Ver. 8.2). Deconvolution of high-resolution C1s and O1s XPS spectra into Gaussian-Lorentzian peak components was performed after calibration of the measured binding energies with the C1s peak and after a Shirley background subtraction.

Optical thickness measurement. Statistical analysis of the thickness distribution of the flakes was performed by implementing a transmission spectral and imaging method[25]. First, transmission spectra of the flakes were obtained by recording the spectra of each individual flake on the borosilicate glass substrate and a flake-free region as reference. The measurements were simply carried out by top illumination of each flake with a broadband halogen lamp followed by collecting the transmitted light with a 60x microscope objective and directing the light towards the spectrometer. Thickness-dependent transmission spectra of the Au flakes were modeled by implementing a self-written MATLAB code based on Matrix theory of multilayer optics[82] and optical constant for single-crystalline Au from Olmon[83] and CRC Handbook[84]. To determine the thickness of the flakes from the transmission spectra, the measured data for each flake was fitted with the models in the 450-750 nm spectral range (see Figure S2a). As the data from the Olmon best matched with the measured spectra of the Au flakes in the fitting region, all the thicknesses reported here were determined based on this model. Next, the optical transmittance of the flakes having different thicknesses was measured by recording the CCD transmission images of the individual flakes from the signals of the green channel, subtracting dark counts and dividing by a reference image from a flake-free region (see Figure S2b). For fast estimation of the thickness values of the flakes from their optical transmittance, a calibration curve was extracted by correlating the thickness values of a large number of flakes obtained with the spectral method to their corresponding transmittance measured from the CCD images, and fitting an exponential function to the resulting data (see Figure S2c). All the reported thicknesses in this work were estimated by simply measuring the optical transmittance from the CCD images of individual flakes and using the fitted calibration curve. The accuracy of this optical approach was validated by performing atomic force microscopy (AFM) measurements, and only a -1 nm deviation was found for the thicknesses obtained with this method (see Figure S2b) compared to those values measured by the AFM technique (see Figure S2d).

Finite-Element Simulation. The finite-element simulations were performed using COMSOL Multiphysics v5.6 to study on the role of space confinemnt effect by modeling the concentration profile of Au(III) ions around two gold flakes growing on a gap-facing surface and a free surface. Simulation details are provided in the Supporting Information 2.

Supporting Information

Additional information about methods of synthesis and characterization of the Au MFs; role of space confinement and halide ions on the Au MFs synthesis; data acquisitions and statistical significance; TEM, EDS, XRD, XPS characterization results of the Au MFs; comparison of Au MFs synthesis methods in terms of maximum area and aspect-ratio.

Acknlowledgements

The authors acknowledge the support of the Swiss National Science Foundation (Eccellenza Grant #194181). The authors also acknowledge the support of the following experimental facilities at EPFL: Interdisciplinary Centre for Electron Microscopy (CIME), and Molecular and Hybrid Materials Characterization Center (MHMC). Finally, the authors would like to thank Dr. Victor Boureau for help with the acquisition of the TEM images and Prof. Joseph S. DuChene for useful feedback on the manuscript.

Author Information

Corresponding Author

Giulia Tagliabue, Ecole Polytechnique Federale de Lausanne (EPFL), Lausanne, Switzerland; orcid.org/0000-0003-4587-728X; Email: giulia.tagliabue@epfl.ch

Other Authors

Fatemeh Kiani, Ecole Polytechnique Federale de Lausanne, Lausanne (EPFL), Switzerland; orcid.org/0000-0002-2707-5251

References

1. Xie, C.; Niu, Z.; Kim, D.; Li, M.; Yang, P., Surface and interface control in nanoparticle catalysis. *Chemical reviews* **2019,** *120* (2), 1184-1249.

2. Xia, Y.; Xiong, Y.; Lim, B.; Skrabalak, S. E., Shape-controlled synthesis of metal nanocrystals: simple chemistry meets complex physics? *Angewandte Chemie International Edition* **2009,** *48* (1), 60-103.

3. Li, C.; Cai, W.; Cao, B.; Sun, F.; Li, Y.; Kan, C.; Zhang, L., Mass synthesis of large, single-crystal Au nanosheets based on a polyol process. *Advanced Functional Materials* **2006,** *16* (1), 83-90.

4. Li, Z.; Liu, Z.; Zhang, J.; Han, B.; Du, J.; Gao, Y.; Jiang, T., Synthesis of single-crystal gold nanosheets of large size in ionic liquids. *The Journal of Physical Chemistry B* **2005,** *109* (30), 14445-14448.

5. Guo, Z.; Zhang, Y.; DuanMu, Y.; Xu, L.; Xie, S.; Gu, N., Facile synthesis of micrometer-sized gold nanoplates through an aniline-assisted route in ethylene glycol solution. *Colloids and Surfaces A: Physicochemical and Engineering Aspects* **2006,** *278* (1-3), 33-38.

6. Ye, S.; Connell, S. D.; McLaughlan, J. R.; Roach, L.; Aslam, Z.; Chankhunthod, N.; Brown, A. P.; Brydson, R.; Bushby, R. J.; Critchley, K., One-Step Preparation of Biocompatible Gold Nanoplates with Controlled Thickness and Adjustable Optical Properties for Plasmon-Based Applications. *Advanced Functional Materials* **2020,** *30* (40), 2003512.

7. Huang, J.-S.; Callegari, V.; Geisler, P.; Brüning, C.; Kern, J.; Prangsma, J. C.; Wu, X.; Feichtner, T.; Ziegler, J.; Weinmann, P., Atomically flat single-crystalline gold nanostructures for plasmonic nanocircuitry. *Nature communications* **2010,** *1* (1), 1-8.

8. Wu, X.; Kullock, R.; Krauss, E.; Hecht, B., Single-crystalline gold microplates grown on substrates by solution-phase synthesis. *Crystal Research and Technology* **2015,** *50* (8), 595-602.

9. Méjard, R.; Verdy, A.; Demichel, O.; Petit, M.; Markey, L.; Herbst, F.; Chassagnon, R.; Colas-des-Francs, G.; Cluzel, B.; Bouhelier, A., Advanced engineering of single-crystal gold nanoantennas. *Optical Materials Express* **2017,** *7* (4), 1157-1168.

10. Hoffmann, B.; Bashouti, M.; Feichtner, T.; Mačković, M.; Dieker, C.; Salaheldin, A.; Richter, P.; Gordan, O.; Zahn, D.; Spiecker, E., New insights into colloidal gold flakes: structural investigation, micro-ellipsometry and thinning procedure towards ultrathin monocrystalline layers. *Nanoscale* **2016,** *8* (8), 4529-4536.

11. Wang, J.; Yu, K.; Yang, Y.; Hartland, G. V.; Sader, J. E.; Wang, G. P., Strong vibrational coupling in room temperature plasmonic resonators. *Nature communications* **2019,** *10* (1), 1-8.

12. Primo, A.; Esteve-Adell, I.; Coman, S. N.; Candu, N.; Parvulescu, V. I.; Garcia, H., One-Step Pyrolysis Preparation of 1.1. 1 Oriented Gold Nanoplatelets Supported on Graphene and Six Orders of Magnitude Enhancement of the Resulting Catalytic Activity. *Angewandte Chemie* **2016,** *128* (2), 617-622.

13. Luc, W.; Fu, X.; Shi, J.; Lv, J.-J.; Jouny, M.; Ko, B. H.; Xu, Y.; Tu, Q.; Hu, X.; Wu, J., Two-dimensional copper nanosheets for electrochemical reduction of carbon monoxide to acetate. *Nature Catalysis* **2019,** *2* (5), 423-430.

14. Xia, X.; Rycenga, M.; Qin, D.; Xia, Y., A silver nanocube on a gold microplate as a well-defined and highly active substrate for SERS detection. *Journal of Materials Chemistry C* **2013,** *1* (38), 6145-6150.

15. Kullock, R.; Ochs, M.; Grimm, P.; Emmerling, M.; Hecht, B., Electrically-driven Yagi-Uda antennas for light. *Nature communications* **2020,** *11* (1), 1-7.

16. Chen, K.; Razinskas, G.; Vieker, H.; Gross, H.; Wu, X.; Beyer, A.; Gölzhäuser, A.; Hecht, B., High-Q, low-mode-volume and multiresonant plasmonic nanoslit cavities fabricated by helium ion milling. *Nanoscale* **2018,** *10* (36), 17148-17155.

17. Todoroki, N.; Tei, H.; Tsurumaki, H.; Miyakawa, T.; Inoue, T.; Wadayama, T., Surface atomic arrangement dependence of electrochemical CO2 reduction on Gold: online electrochemical mass spectrometric study on low-index au (hkl) surfaces. *ACS Catalysis* **2019,** *9* (2), 1383-1388.

18. Sá, J.; Tagliabue, G.; Friedli, P.; Szlachetko, J.; Rittmann-Frank, M. H.; Santomauro, F. G.; Milne, C. J.; Sigg, H., Direct observation of charge separation on Au localized surface plasmons. *Energy & Environmental Science* **2013,** *6* (12), 3584-3588.

19. DuChene, J. S.; Tagliabue, G.; Welch, A. J.; Cheng, W.-H.; Atwater, H. A., Hot hole collection and photoelectrochemical CO2 reduction with plasmonic Au/p-GaN photocathodes. *Nano letters* **2018,** *18* (4), 2545-2550.

20. Kaltenecker, K. J.; Krauss, E.; Casses, L.; Geisler, M.; Hecht, B.; Mortensen, N. A.; Jepsen, P. U.; Stenger, N., Mono-crystalline gold platelets: a high-quality platform for surface plasmon polaritons. *Nanophotonics* **2020,** *9* (2), 509-522.

21. Qin, H. L.; Wang, D.; Huang, Z. L.; Wu, D. M.; Zeng, Z. C.; Ren, B.; Xu, K.; Jin, J., Thickness-controlled synthesis of ultrathin Au sheets and surface plasmonic property. *Journal of the American Chemical Society* **2013,** *135* (34), 12544-12547.

22. Tsai, D.-H.; Davila-Morris, M.; DelRio, F. W.; Guha, S.; Zachariah, M. R.; Hackley, V. A., Quantitative determination of competitive molecular adsorption on gold nanoparticles using attenuated total reflectance–Fourier transform infrared spectroscopy. *Langmuir* **2011,** *27* (15), 9302-9313.

23. Mudunkotuwa, I. A.; Al Minshid, A.; Grassian, V. H., ATR-FTIR spectroscopy as a tool to probe surface adsorption on nanoparticles at the liquid–solid interface in environmentally and biologically relevant media. *Analyst* **2014,** *139* (5), 870-881.

24. Cortés, E.; Besteiro, L. V.; Alabastri, A.; Baldi, A.; Tagliabue, G.; Demetriadou, A.; Narang, P., Challenges in plasmonic catalysis. *ACS nano* **2020,** *14* (12), 16202-16219.

25. Großmann, S.; Friedrich, D.; Karolak, M.; Kullock, R.; Krauss, E.; Emmerling, M.; Sangiovanni, G.; Hecht, B., Nonclassical optical properties of mesoscopic gold. *Physical review letters* **2019,** *122* (24), 246802.

26. V. Grayli, S.; Zhang, X.; MacNab, F. C.; Kamal, S.; Star, D.; Leach, G. W., Scalable, green fabrication of single-crystal noble metal films and nanostructures for low-loss nanotechnology applications. *ACS nano* **2020,** *14* (6), 7581-7592.

27. Sundararaman, R.; Narang, P.; Jermyn, A. S.; Goddard III, W. A.; Atwater, H. A., Theoretical predictions for hot-carrier generation from surface plasmon decay. *Nature communications* **2014,** *5* (1), 1-8.

28. Tagliabue, G.; Jermyn, A. S.; Sundararaman, R.; Welch, A. J.; DuChene, J. S.; Pala, R.; Davoyan, A. R.; Narang, P.; Atwater, H. A., Quantifying the role of surface plasmon excitation and hot carrier transport in plasmonic devices. *Nature communications* **2018,** *9* (1), 1-8.

29. Tagliabue, G.; DuChene, J. S.; Abdellah, M.; Habib, A.; Gosztola, D. J.; Hattori, Y.; Cheng, W.-H.; Zheng, K.; Canton, S. E.; Sundararaman, R., Ultrafast hot-hole injection modifies hot-electron dynamics in Au/p-GaN heterostructures. *Nature Materials* **2020,** *19* (12), 1312-1318.

30. Sajanlal, P. R.; Pradeep, T., Electric-Field-Assisted Growth of Highly Uniform and Oriented Gold Nanotriangles on Conducting Glass Substrates. *Advanced Materials* **2008,** *20* (5), 980-983.
31. Zhai, Y.; DuChene, J. S.; Wang, Y.-C.; Qiu, J.; Johnston-Peck, A. C.; You, B.; Guo, W.; DiCiaccio, B.; Qian, K.; Zhao, E. W., Polyvinylpyrrolidone-induced anisotropic growth of gold nanoprisms in plasmon-driven synthesis. *Nature materials* **2016,** *15* (8), 889-895.
32. Guo, W.; Johnston-Peck, A. C.; Zhang, Y.; Hu, Y.; Huang, J.; Wei, W. D., Cooperation of hot holes and surface adsorbates in plasmon-driven anisotropic growth of gold nanostars. *Journal of the American Chemical Society* **2020,** *142* (25), 10921-10925.
33. Radha, B.; Kulkarni, G., A real time microscopy study of the growth of giant Au microplates. *Crystal growth & design* **2011,** *11* (1), 320-327.
34. Lv, L.; Wu, X.; Yang, Y.; Han, X.; Mezzenga, R.; Li, C., Trans-scale 2D synthesis of millimeter-large Au single crystals via silk fibroin templates. *ACS Sustainable Chemistry & Engineering* **2018,** *6* (9), 12419-12425.
35. Zhou, J.; Saha, A.; Adamcik, J.; Hu, H.; Kong, Q.; Li, C.; Mezzenga, R., Macroscopic single-crystal gold microflakes and their devices. *Advanced Materials* **2015,** *27* (11), 1945-1950.
36. Ali Umar, A.; Oyama, M.; Mat Salleh, M.; Yeop Majlis, B., Formation of highly thin, electron-transparent gold nanoplates from nanoseeds in ternary mixtures of cetyltrimethylammonium bromide, poly (vinyl pyrrolidone), and poly (ethylene glycol). *Crystal growth & design* **2010,** *10* (8), 3694-3698.
37. Krauss, E.; Kullock, R.; Wu, X.; Geisler, P.; Lundt, N.; Kamp, M.; Hecht, B., Controlled growth of high-aspect-ratio single-crystalline gold platelets. *Crystal Growth & Design* **2018,** *18* (3), 1297-1302.
38. DuChene, J. S.; Niu, W.; Abendroth, J. M.; Sun, Q.; Zhao, W.; Huo, F.; Wei, W. D., Halide anions as shape-directing agents for obtaining high-quality anisotropic gold nanostructures. *Chemistry of Materials* **2013,** *25* (8), 1392-1399.
39. Ghosh, S.; Manna, L., The many “facets” of halide ions in the chemistry of colloidal inorganic nanocrystals. *Chemical reviews* **2018,** *118* (16), 7804-7864.
40. Kim, M. J.; Cruz, M. A.; Chen, Z.; Xu, H.; Brown, M.; Fichthorn, K. A.; Wiley, B. J., Isotropic Iodide Adsorption Causes Anisotropic Growth of Copper Microplates. *Chemistry of Materials* **2020,** *33* (3), 881-891.
41. Rai, A.; Singh, A.; Ahmad, A.; Sastry, M., Role of halide ions and temperature on the morphology of biologically synthesized gold nanotriangles. *Langmuir* **2006,** *22* (2), 736-741.
42. Lee, J. W.; Han, J.; Lee, D. S.; Bae, S.; Lee, S. H.; Lee, S. K.; Moon, B. J.; Choi, C. J.; Wang, G.; Kim, T. W., 2D Single-Crystalline Copper Nanoplates as a Conductive Filler for Electronic Ink Applications. *Small* **2018,** *14* (8), 1703312.
43. Kumar, D. R.; Kulkarni, A. A.; Prasad, B., Synthesis of triangular gold nanoplates: Role of bromide ion and temperature. *Colloids and Surfaces A: Physicochemical and Engineering Aspects* **2013,** *422*, 181-190.
44. Moiraghi, R.; Douglas-Gallardo, O. A.; Coronado, E. A.; Macagno, V. A.; Perez, M. A., Gold nucleation inhibition by halide ions: a basis for a seed-mediated approach. *Rsc Advances* **2015,** *5* (25), 19329-19336.
45. Chen, L.; Ji, F.; Xu, Y.; He, L.; Mi, Y.; Bao, F.; Sun, B.; Zhang, X.; Zhang, Q., High-yield seedless synthesis of triangular gold nanoplates through oxidative etching. *Nano letters* **2014,** *14* (12), 7201-7206.
46. Soejima, T.; Kimizuka, N., One-pot room-temperature synthesis of single-crystalline gold nanocorolla in water. *Journal of the American Chemical Society* **2009,** *131* (40), 14407-14412.
47. Radha, B.; Kulkarni, G., Giant single crystalline Au microplates. *Current science* **2012**, 70-77.
48. Tian, Z.; Wei, C.; Sun, J., Recent advances in the template-confined synthesis of two-dimensional materials for aqueous energy storage devices. *Nanoscale Advances* **2020,** *2* (6), 2220-2233.
49. Zheng, Z.; Yao, J.; Li, J.; Yang, G., Non-layered 2D materials toward advanced photoelectric devices: progress and prospects. *Materials Horizons* **2020,** *7* (9), 2185-2207.

50. Gao, X.; Lu, F.; Dong, B.; Zhou, T.; Tian, W.; Zheng, L., Zwitterionic vesicles with AuCl 4− counterions as soft templates for the synthesis of gold nanoplates and nanospheres. *Chemical Communications* **2014,** *50* (63), 8783-8786.

51. Saito, Y.; Luo, X.; Zhao, C.; Pan, W.; Chen, C.; Gong, J.; Matsumoto, H.; Yao, J.; Wu, H., Filling the gaps between graphene oxide: A general strategy toward nanolayered oxides. *Advanced Functional Materials* **2015,** *25* (35), 5683-5690.

52. Wu, J.; Ma, L.; Samanta, A.; Liu, M.; Li, B.; Yang, Y.; Yuan, J.; Zhang, J.; Gong, Y.; Lou, J., Growth of molybdenum carbide–graphene hybrids from molybdenum disulfide atomic layer template. *Advanced Materials Interfaces* **2017,** *4* (4), 1600866.

53. Huang, W.; Gan, L.; Yang, H.; Zhou, N.; Wang, R.; Wu, W.; Li, H.; Ma, Y.; Zeng, H.; Zhai, T., Controlled synthesis of ultrathin 2D β-In2S3 with broadband photoresponse by chemical vapor deposition. *Advanced Functional Materials* **2017,** *27* (36), 1702448.

54. Zhou, S.; Wang, R.; Han, J.; Wang, D.; Li, H.; Gan, L.; Zhai, T., Ultrathin non-van der Waals magnetic Rhombohedral Cr2S3: space-confined chemical vapor deposition synthesis and raman scattering investigation. *Advanced Functional Materials* **2019,** *29* (3), 1805880.

55. Gong, C.; Chu, J.; Yin, C.; Yan, C.; Hu, X.; Qian, S.; Hu, Y.; Hu, K.; Huang, J.; Wang, H., Self-confined growth of ultrathin 2D nonlayered wide-bandgap semiconductor CuBr flakes. *Advanced Materials* **2019,** *31* (36), 1903580.

56. Guo, Z.; Zhang, Y.; Xu, A.; Wang, M.; Huang, L.; Xu, K.; Gu, N., Layered assemblies of single crystal gold nanoplates: direct room temperature synthesis and mechanistic study. *The Journal of Physical Chemistry C* **2008,** *112* (33), 12638-12645.

57. Straney, P. J.; Diemler, N. A.; Smith, A. M.; Eddinger, Z. E.; Gilliam, M. S.; Millstone, J. E., Ligand-mediated deposition of noble metals at nanoparticle plasmonic hotspots. *Langmuir* **2018,** *34* (3), 1084-1091.

58. Tang, Z.; Kwon, H.; Yi, M.; Kim, K.; Han, J. W.; Kim, W. S.; Yu, T., Role of halide ions for controlling morphology of copper nanocrystals in aqueous solution. *ChemistrySelect* **2017,** *2* (17), 4655-4661.

59. Stefancu, A.; Lee, S.; Zhu, L.; Liu, M.; Lucacel, R. C.; Cortés, E.; Leopold, N., Fermi Level Equilibration at the Metal–Molecule Interface in Plasmonic Systems. *Nano Letters* **2021,** *21* (15), 6592-6599.

60. Xin, W.; Severino, J.; De Rosa, I. M.; Yu, D.; Mckay, J.; Ye, P.; Yin, X.; Yang, J.-M.; Carlson, L.; Kodambaka, S., One-step synthesis of tunable-size gold nanoplates on graphene multilayers. *Nano letters* **2018,** *18* (3), 1875-1881.

61. Lin, W.-H.; Lu, Y.-H.; Hsu, Y.-J., Au nanoplates as robust, recyclable SERS substrates for ultrasensitive chemical sensing. *Journal of colloid and interface science* **2014,** *418*, 87-94.

62. Aherne, D.; Ledwith, D. M.; Gara, M.; Kelly, J. M., Optical properties and growth aspects of silver nanoprisms produced by a highly reproducible and rapid synthesis at room temperature. *Advanced Functional Materials* **2008,** *18* (14), 2005-2016.

63. Kan, C.; Zhu, X.; Wang, G., Single-crystalline gold microplates: synthesis, characterization, and thermal stability. *The Journal of Physical Chemistry B* **2006,** *110* (10), 4651-4656.

64. Germain, V.; Li, J.; Ingert, D.; Wang, Z.; Pileni, M., Stacking faults in formation of silver nanodisks. *The Journal of Physical Chemistry B* **2003,** *107* (34), 8717-8720.

65. Chen, S.; Xu, P.; Li, Y.; Xue, J.; Han, S.; Ou, W.; Li, L.; Ni, W., Rapid seedless synthesis of gold nanoplates with microscaled edge length in a high yield and their application in SERS. *Nano-micro letters* **2016,** *8* (4), 328-335.

66. Golze, S. D.; Hughes, R. A.; Rouvimov, S.; Neal, R. D.; Demille, T. B.; Neretina, S., Plasmon-mediated synthesis of periodic arrays of gold nanoplates using substrate-immobilized seeds lined with planar defects. *Nano letters* **2019,** *19* (8), 5653-5660.

67. Ha, T. H.; Koo, H.-J.; Chung, B. H., Shape-controlled syntheses of gold nanoprisms and nanorods influenced by specific adsorption of halide ions. *The Journal of Physical Chemistry C* **2007,** *111* (3), 1123-1130.

68. Magnussen, O. M., Ordered anion adlayers on metal electrode surfaces. *Chemical reviews* **2002,** *102* (3), 679-726.

69. Meena, S. K.; Celiksoy, S.; Schäfer, P.; Henkel, A.; Sönnichsen, C.; Sulpizi, M., The role of halide ions in the anisotropic growth of gold nanoparticles: a microscopic, atomistic perspective. *Physical Chemistry Chemical Physics* **2016,** *18* (19), 13246-13254.

70. Armstrong, J.; Pylant, E.; White, J., Thermal chemistry of biacetyl on Si (100). *Journal of Vacuum Science & Technology A: Vacuum, Surfaces, and Films* **1998,** *16* (1), 123-130.

71. Popat, K. C.; Sharma, S.; Desai, T. A., Quantitative XPS analysis of PEG-modified silicon surfaces. *The Journal of Physical Chemistry B* **2004,** *108* (17), 5185-5188.

72. Pylant, E.; Hubbard, M.; White, J., Thermal and Low-Energy Electron-Driven Chemistry of Biacetyl on Ag (111). *The Journal of Physical Chemistry* **1996,** *100* (39), 15890-15899.

73. Wang, C.; Kan, C.; Zhu, J.; Zeng, X.; Wang, X.; Li, H.; Shi, D., Synthesis of high-yield gold nanoplates: fast growth assistant with binary surfactants. *Journal of Nanomaterials* **2010,** *2010*.

74. Chatterjee, D.; Kamalnath, K.; Ahmad, R.; Singh, A. K.; Ravishankar, N., Orientation selection during heterogeneous nucleation: implications for heterogeneous catalysis. *The Journal of Physical Chemistry C* **2017,** *121* (18), 10027-10037.

75. Marks, L., Experimental studies of small particle structures. *Reports on Progress in Physics* **1994,** *57* (6), 603.

76. Callister, W. D.; Rethwisch, D. G., *Materials science and engineering: an introduction*. Wiley New York: 2018; Vol. 9.

77. Pérez-Juste, J.; Liz-Marzán, L. M.; Carnie, S.; Chan, D. Y.; Mulvaney, P., Electric-field-directed growth of gold nanorods in aqueous surfactant solutions. *Advanced Functional Materials* **2004,** *14* (6), 571-579.

78. Venkatasubramanian, R.; He, J.; Johnson, M. W.; Stern, I.; Kim, D. H.; Pesika, N. S., Additive-mediated electrochemical synthesis of platelike copper crystals for methanol electrooxidation. *Langmuir* **2013,** *29* (43), 13135-13139.

79. Elding, L. I.; Groning, A., Kinetics, mechanism and equilibria for halide substitution processes of chloro bromo complexes of gold (III). *Acta Chem. Scand* **1978,** *32* (9), 867-877.

80. Dahanayaka, D. H.; Wang, J. X.; Hossain, S.; Bumm, L. A., Optically transparent Au {111} substrates: Flat gold nanoparticle platforms for high-resolution scanning tunneling microscopy. *Journal of the American Chemical Society* **2006,** *128* (18), 6052-6053.

81. Qin, Y.; Song, Y.; Huang, T.; Qi, L., Ionic liquid-assisted synthesis of thorned gold plates comprising three-branched nanotip arrays. *Chemical Communications* **2011,** *47* (10), 2985-2987.

82. Born, M.; Wolf, E., *Principles of optics: electromagnetic theory of propagation, interference and diffraction of light*. Elsevier: 2013.

83. Olmon, R. L.; Slovick, B.; Johnson, T. W.; Shelton, D.; Oh, S.-H.; Boreman, G. D.; Raschke, M. B., Optical dielectric function of gold. *Physical Review B* **2012,** *86* (23), 235147.

84. Weber, M. J., *Handbook of optical materials*. CRC press: 2002; Vol. 19.

Tabale of Contents Graphic